

Low transverse momentum photon production in proton-nucleus collisions at 18 GeV/c

M. L. Tincknell*

Purdue University, West Lafayette, Indiana 47907-1396

R. L. Clark

Vanderbilt University, Nashville, Tennessee 37235

C. Woody, D. Lissauer, and H. Takai

Brookhaven National Laboratory, Upton, New York 11973

A. Ray*

Variable Energy Cyclotron Centre, 1/AF, Bidhannagar, Calcutta 700064, India

J. Gomez del Campo and D. Shapira

Oak Ridge National Laboratory, Oak Ridge, Tennessee 37831

C. Erd,[†] J. Schukraft, and W. Willis[‡]

CERN, Geneva, Switzerland

(Received 15 April 1996)

Inclusive single photon spectra have been measured in the transverse momentum (p_T) range from a few MeV/c up to approximately 1 GeV/c at various nucleon-nucleon center of momentum rapidities (y_{NN}) in the interval from $-2.4 < y_{NN} < +0.5$ in 18 GeV/c p -Be and p -W collisions. These distributions were used to estimate the inclusive p_T and rapidity distributions for π^0 production over approximately the same kinematic range. The measured photon spectra are compared with the expected distribution of photons from π^0 decays and hadronic bremsstrahlung in order to search for new sources of "soft" photons at low transverse momentum. The results indicate no anomalous sources of soft photons in either p -Be or p -W interactions at these energies. The p -W data at forward angles set a limit on any excess of low p_T photons at < 2.65 times hadronic bremsstrahlung at the 99% C.L. [S0556-2813(96)06110-9]

PACS number(s): 13.85.Qk, 13.40.-f, 25.40.Ve, 25.75.-q

I. INTRODUCTION

The study of photon production in hadron collisions has historically provided new insights into hadronic processes which are often difficult to measure by other means. One reason for this is that photons, as well as lepton pairs produced by the decay of virtual photons, are penetrating probes of hadronic matter that can escape from the interaction region with a low probability of secondary interaction. These electromagnetic probes can therefore provide information about all stages of the collision, including the very early stage before hadronization has occurred. The initial hard scattering of partons can lead to high transverse momentum (p_T) direct photon production via the subprocesses of QCD Compton scattering ($qg \rightarrow \gamma q$) and quark-antiquark annihilation ($q\bar{q} \rightarrow \gamma g$). This phenomenon has been studied in detail

in $p-p$ and $p-\bar{p}$ interactions [1], and has recently been investigated in nucleus-nucleus collisions [2].

The production of direct single photons at low p_T occurs via the same fundamental processes as at high p_T , except that the constituents involved carry only a small fraction of the initial particle momenta. In addition, soft $q\bar{q}$ pairs produced during the collision may enhance the yield of direct photons at low p_T [3,4]. One experiment, carried out at the BEBC bubble chamber at CERN [5], reported an excess of photon production at very small x_F and low p_T at a level five times greater than that expected from hadronic bremsstrahlung in K^+-p interactions at 70 GeV/c. More recent data by the same group confirmed this effect in π^+-p and K^+-p reactions at 250 GeV/c [6]. This result is particularly surprising, since in the low p_T limit, the production rate of photons from hadronic bremsstrahlung can be calculated classically [7,8]. It is therefore suggestive of some other source of soft photons, such as bremsstrahlung due to pion rescattering in nuclear matter [9], or some new mechanism such as in certain soft annihilation models [10], or models that involve the formation of dense regions of cold quark-gluon plasma [11].

Other experiments have also reported an excess of low p_T photons in K^+-p interactions at 32 GeV/c [12], in $\mu-p$ interactions at 200 GeV/c [13], and in π^-p inter-

*Former address: Oak Ridge National Laboratory and The Joint Institute for Heavy-Ion Research, University of Tennessee, Oak Ridge, TN 37831.

[†]Present address: European Space Agency, Astrophysics Division, Noordwijk, The Netherlands.

[‡]Present address: Columbia University, New York, NY 10027.

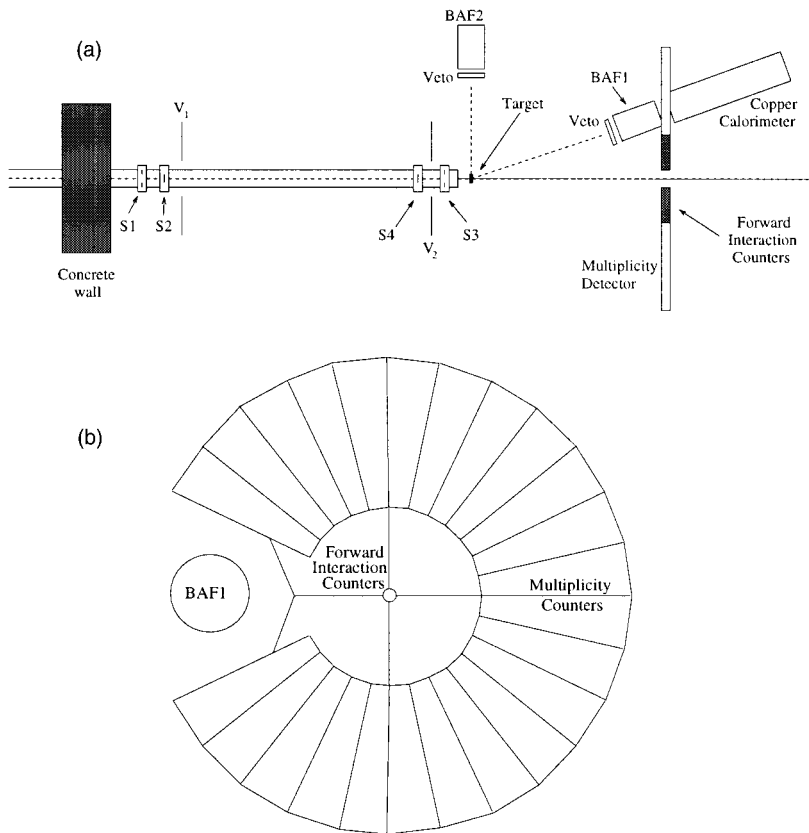


FIG. 1. Plan view of the E855 detector setup in the AGS E814 beam area (a), and elevation view (looking downstream from the target) of the BAF1 BaF₂ detector, the charged multiplicity scintillator array, and the forward interaction counters (b).

actions at 280 GeV/c [14]. However, still other experiments have observed that the photon yield at low p_T is consistent with that originating from π^0 decays and hadronic bremsstrahlung [15–18]. The recent results by the HELIOS group [18], which used the same technique and one of the same detectors as this experiment, reported a small excess of photons above the level of hadronic bremsstrahlung that was within their systematic errors.

The related process of lepton pair (virtual photon) production has also had a long history of study in hadronic interactions. Many experiments covering a wide kinematic range have observed an excess of low mass lepton pairs in the 200–600 MeV/c² mass region that cannot be readily explained by known mechanisms [19]. The excesses in low p_T photons and low mass lepton pairs can be linked semi-quantitatively by plotting them as a function of transverse mass ($m_T = \sqrt{p_T^2/c^2 + m_{l+l-}^2}$) [20]. Recently, it has been shown that these anomalous low mass lepton pairs can possibly be explained by η Dalitz decays [21]. However, the origin of an excess of low mass lepton pairs in heavy ion collisions still remains unclear [22].

The results reported here were obtained from AGS Experiment E855 carried out at Brookhaven National Laboratory during the spring of 1990. The experiment was designed to measure photon production in the p_T range from a few MeV/c up to several GeV/c in proton-nucleus collisions at 18 GeV/c, and was the first dedicated experiment to study this phenomenon in this beam energy range. This paper presents the final results on the analysis of the p -Be and p -W data at 18 GeV/c (preliminary results have previously been reported on p -Be interactions [23]). The experimental setup

will be described first, then the data analysis and corrections to the data, followed by a presentation of the inclusive photon spectra at various rapidities, and a determination of the π^0 p_T and rapidity distributions that were derived from these data. Then the various sources of background to the inclusive photon spectra at low p_T will be discussed, after which the residual low p_T photon spectra will be presented. Finally, a summary of the results and conclusions will be given.

II. DESCRIPTION OF THE EXPERIMENT

The layout of the detectors used in E855 is shown in Fig. 1. The experiment was carried out within the framework of the E814 heavy ion spectrometer at the Brookhaven AGS, which served as a host, providing beam instrumentation, trigger logic, data acquisition, and online monitoring. The detectors were arranged in an open geometry downstream and to one side of the target, with a minimum amount of surrounding material in order to minimize the probability of secondary interactions which could produce low energy photons. Two barium fluoride (BaF₂) scintillation detectors were used to measure photons over a large rapidity range. Both BAF detectors were moved to various polar angles to cover different rapidities. The first (BAF1) covered the nucleon-nucleon center of momentum rapidity (y_{NN}) range from +0.5 to -1.0 in five steps (laboratory angles 11°, 18°, 30°, 39°, 47°), while the second (BAF2) covered the rapidity range from -1.3 to -2.4 in five additional steps (lab angles 60°, 75°, 90°, 105°, 120°). Table I gives a list of the rapidity coverage and the laboratory angle settings for each detector. A large array of 24 wedged-shaped plastic scintillation

TABLE I. Nominal nucleon-nucleon center of momentum rapidity, rapidity coverage interval, and laboratory angle settings for the two BAF detectors. The central 7 crystals of the BAF detectors covered an average angular range of $\Delta\theta_{\text{lab}} = \pm 3.35^\circ$.

Detector	Nominal y_{NN}	Δy_{NN}	Lab angle
BAF1	+0.5	0.66	11°
BAF1	0.0	0.39	18°
BAF1	-0.5	0.24	30°
BAF1	-0.8	0.20	39°
BAF1	-1.0	0.16	47°
BAF2	-1.3	0.13	60°
BAF2	-1.6	0.12	75°
BAF2	-1.8	0.12	90°
BAF2	-2.1	0.12	105°
BAF2	-2.4	0.12	120°

counters was used to trigger on collisions with at least one charged particle in the central rapidity region, and to provide a measure of the overall charged particle multiplicity in the event. The array, shown in Fig. 1, covered the rapidity range $-0.5 < y_{NN} < +0.5$ and an azimuthal angle of approximately 300 degrees. In addition, four small scintillation counters were used to detect charged particles at $y_{NN} \geq 0.5$, which were used together with the multiplicity array to veto multiple interactions that were close together in time. A small, four interaction length deep hadron calorimeter located at $y_{NN} = 0$ was used to study the response of the BaF₂ detectors to high energy neutrons.

A. Barium fluoride arrays

Barium fluoride was chosen as the photon detector material because of the extremely short decay time of its fast component (≤ 1 ns), and the high light output of its slow component. Barium fluoride has a density of $\rho = 4.89$ g/cm³, a hadronic interaction length of $\lambda = 29.9$ cm, a radiation length of $X_0 = 2.05$ cm, and a Molière radius of $R_M = 3.4$ cm. The fast rise time (< 1 ns) of the fast compo-

nent provided good time resolution for time-of-flight (TOF) measurements, which was used to reject out-of-time backgrounds, such as photons not originating from the target, low energy neutrons, and particles produced in the surrounding material. The slow component provided good energy resolution over a large energy range.

Each barium fluoride detector consisted of an array of 19 BaF₂ crystals in a hexagonal closed packed arrangement as shown in Fig. 2. The crystals in BAF1 measured 5 cm from flat-to-flat and were 30 cm (14.3 X_0) long (actually consisting of two separate 15 cm long crystals coupled together), while the crystals in BAF2 measured 6 cm flat-to-flat and were 20 cm (9.5 X_0) long. The crystals were read out with Hamamastu R2059 two inch diameter quartz window photomultiplier tubes. The anode signals from each tube were digitized using Fastbus ADC's (LeCroy 1885F) in both a long (1 μ s) and a short (25 ns) gate and were used for the energy measurement. The dynode signals from each tube were amplified using fast inverting amplifiers (Phillips 777) and sent to constant fraction discriminators (CFD 8001) and Fastbus TDC's (LeCroy 1875), which were used for the timing measurement. BAF1 was located an average distance of 1.4 m from the target, and the central 7 crystals covered an effective area of 0.018 m², or 0.07% of the 4π solid angle. The BAF2 detector was placed an average of 1.5 m from the target, and its central 7 crystals covered an area of 0.028 m², or 0.1% of 4π steradians. The central 7 crystals of the BAF detectors covered an average angular range of $\Delta\theta_{\text{lab}} = \pm 3.35^\circ$. Thin plastic scintillation counters were placed in front of both BaF₂ detectors, which were used in the offline analysis to veto charged particles.

B. Trigger

The incoming beam was defined by the four scintillation counters $S1$, $S2$, $S3$, and $S4$ shown in Fig. 1. Counters $S1$ and $S3$ were veto counters with beam-defining holes of 1.5 and 0.6 cm, respectively, while counters $S2$ and $S4$ counted the on-axis beam particles. Two other large veto counters $V1$ and $V2$ were used to suppress upstream beam interactions. The beam trigger required a single beam particle to

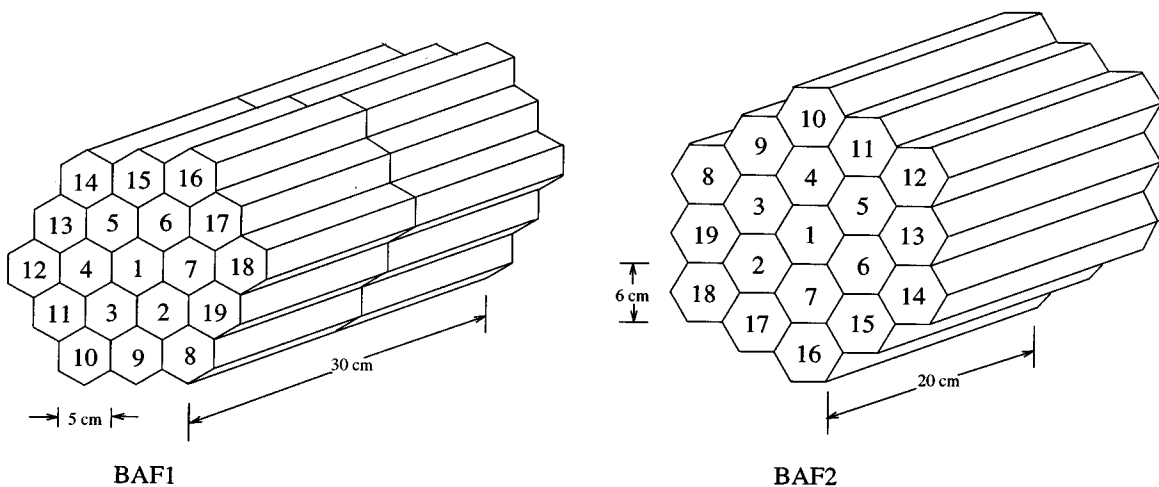


FIG. 2. The E855 barium fluoride photon detectors BAF1 and BAF2.

pass through the beam defining counters with no other particle in any of the veto counters ($\overline{S1} \cdot \overline{S2} \cdot \overline{S3} \cdot \overline{S4} \cdot \overline{V1} \cdot \overline{V2}$). An event producing a trigger was vetoed by any other interaction within $\pm 2 \mu\text{s}$ before or after the time of the trigger.

The thickness of both the Be and W targets was 1% of a proton interaction length, 5 mm for Be and 1 mm for W. Interactions were defined by a pretrigger which required at least one of the charged multiplicity array elements to fire along with a valid beam trigger. The trigger for the BAF detectors required the energy deposited in either BAF1 or BAF2 to be greater than a certain threshold, which was typically $\sim 10 \text{ MeV}$ ($p_T \approx 3 \text{ MeV}/c$ at $y_{NN}=0$). The veto counters in front of each BAF detector were not used in the trigger, so both charged and neutral events were accepted. The selection of neutral events was made in the offline data selection as described below. The events in which a charged particle fired the veto counters provided a sample of minimum ionizing particles, which were used for energy calibration and monitoring. Approximately 24×10^6 events were collected for all types of triggers, of which 16×10^6 were charged and neutral events in the two BAF detectors.

III. DATA SELECTION AND ANALYSIS

In the offline analysis, neutral events were selected in either BAF1 or BAF2 by requiring no charged particle fire the veto counter in front of the corresponding detector. The crystal with the maximum energy was required to be one of the seven central crystals of the array, which minimized the effects of side leakage and interactions in the canister and stand surrounding the crystals. In addition, the energies measured in the short and long ADC gates were required to be consistent with that of a good BaF_2 signal. It was assumed that all the energy in the detector originated from a single photon shower. The photon energy was obtained by the sum of the energy from the crystal containing the maximum energy, and the 6 surrounding crystals. The shower position within the detector was determined using a logarithmic weighting procedure [24] which gave a resolution of $\sim 7.1 \text{ mm}$ in BAF1 and $\sim 10.8 \text{ mm}$ in BAF2.

A. Energy calibration and resolution

Events in which a charged particle fired the veto counter in front of either BAF detector provided a sample of minimum ionizing particles that were used for energy calibration. A minimum ionizing particle traversing the 30 cm long crystals in BAF1 produced a peak which corresponded to a most probable energy loss of 200 MeV, and to 133 MeV for the 20 cm crystals in BAF2. These were used to determine the energy scale in both detectors and to monitor gain variations throughout the run.

The energy resolution of BAF1 varied from about 15% at 6 MeV to 1.6% at 4 GeV, and could be parameterized as $\sigma_E/E = 3.2\%/\sqrt{E/(1 \text{ GeV})}$ [18]. At higher energies (generally for $p_T \geq 0.2 \text{ GeV}$), back leakage was significant in both detectors, but more so for BAF2 than for BAF1 because of the shorter length of the crystals. For this reason, BAF2 was used at the more backward rapidities where the photon energies were lower. However, correction factors were applied to the measured energy in both detectors to correct for the back

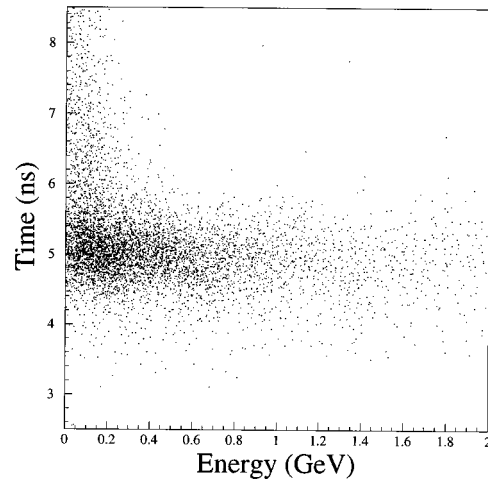


FIG. 3. Slewing corrected time vs energy for a typical BAF1 crystal.

leakage. For BAF1, a multiplicative correction factor was determined by computing a shift to the measured energy given by $\Delta E/E_{\text{peak}} = a_1 + a_2 \ln(E_{\text{peak}})$, where the constants a_1 and a_2 were determined by simulations using GEANT [25]. For BAF2, a more complicated correction was necessary, in which the photon energy was selected randomly from the probability distribution of photon energies that could produce the measured energy in the detector. These distributions were computed using a procedure based on GEANT which is described in detail in Ref. [26].

B. Time resolution and trigger efficiency

Timing information was used to identify photons originating from the target and to reject out-of-time photons and slow neutrons. The event time in each BAF detector was taken from the TDC of the crystal which had the maximum energy. Although constant fraction discriminators (CFD's) were used to minimize the effect of time slewing during data taking, an offline time slewing correction, described in Ref. [26], was applied to BAF1 in order to improve its time resolution. No correction was applied to BAF2 because the range in amplitude of the signals was much less than BAF1. Figure 3 shows a typical slewing-corrected time versus energy plot for BAF1. A prompt photon peak can be seen at approximately 5 ns along with a low energy background that occurs at later times. A Gaussian fit to the early-time side of the photon peak, averaged over all energies, gave a fitted Gaussian parameter σ (rms variation) of approximately 420 ps. A cut at 500 ps was applied to the later-time side of the peak to reject the out-of-time backgrounds. Assuming the photon peak is purely Gaussian, the one-sided cut from $+1.2\sigma$ to infinity rejects 12% of the valid photon events, which was corrected later in the analysis.

The timing signals from the CFD's also provided the trigger from each of the BAF detectors. At low energies, it was necessary to correct the data for the trigger efficiencies of the CFD's. The probability for a discriminator signal to be above threshold (producing a valid TDC signal) was determined as a function of energy by using real data. The efficiency for each individual crystal was obtained from events when it was

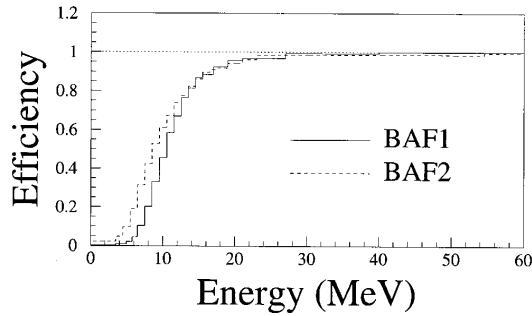


FIG. 4. Probability of triggering the discriminator of the crystal with the maximum energy as a function of the total photon energy.

one of the 6 crystals surrounding the crystal with the maximum energy. A GEANT simulation was then used to combine these probabilities to give an overall detection efficiency as a function of the total photon energy [26]. The resulting efficiency curves for BAF1 and BAF2 are shown in Fig. 4. The data were corrected for these efficiencies with a weighting factor ranging from 5 at the lowest energy ($E \approx 6-8$ MeV) to 1 at energies greater than ~ 20 MeV.

C. Target out subtraction

The data were corrected for nontarget related backgrounds by subtracting appropriately scaled target-out data from the normal 1% beryllium and tungsten data at each rapidity. A small amount of data was also taken with 2% and 5% targets in order to study the level of secondary interactions in the target. A linear extrapolation of the 5%-2%-1% spectra showed good agreement with the actual target-out spectrum for the beryllium data. However, because of the short radiation length of tungsten ($X_0 = 0.35$ cm), secondary interactions in the target were a significant source of background in the tungsten data, particularly at rapidities corresponding to 90° in the laboratory, where the photons went nearly sideways through the 0.72 cm radius of the target. This gave rise to a large background from secondary photons in the p -W data at low p_T . The treatment of this background and its contribution to the systematic error on the residual low p_T photon spectrum are discussed in a later section.

D. Charged multiplicity requirements

Although only one paddle of the charged multiplicity detector was required to fire at the online trigger level, a requirement was made that two paddles fire ($n_{\text{ch}} \geq 2$) in the offline analysis. This was done to suppress backgrounds arising from accidental hits in the charged multiplicity array. This cut was particularly important for the data at forward rapidities, where this background (presumably from beam-halo) made a significant contribution to the low p_T photon spectrum. This is shown in Fig. 5 for $y_{NN} = +0.5$, where the charged multiplicity one events are seen to have a large low p_T peak relative to events with $n_{\text{ch}} \geq 2$. The energy of these photons in the lab extended above 100 MeV, which, combined with the fact that the same effect was observed in the p -Be data, precludes the explanation that these photons result from giant dipole resonance decays of heavy nuclei excited by peripheral (low multiplicity) interactions.

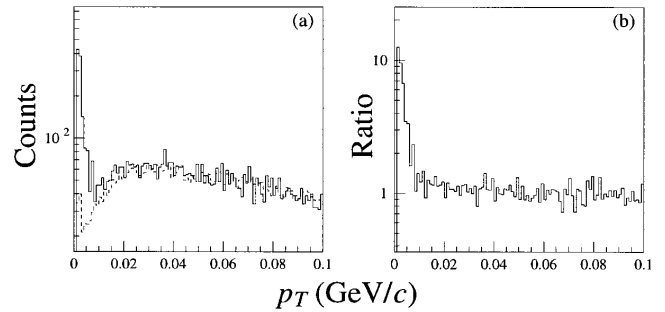


FIG. 5. Comparison of events with $n_{\text{ch}}=1$ for p -W data. The solid curve in (a) shows the p -W p_T spectrum at $y_{NN}=0.5$ for all charged particle multiplicities, and the dashed curve shows the p_T spectrum after rejecting the events associated with $n_{\text{ch}}=1$ (and scaling back up to the full data). Panel (b) shows the ratio of these two curves.

E. Corrections to the data

Following the event selection, the data were corrected for geometrical acceptance, energy leakage, trigger efficiency, time of flight cut, and empty target subtraction. A factor was also applied to correct for the $n_{\text{ch}} \geq 2$ cut in the charged multiplicity detector. This factor, which was independent of p_T , was approximately 1.7 for the p -W data and 3.3 for the p -Be data, corresponding to the selection of roughly 60% and 30% of the total cross sections for the two different targets. In addition, rapidity-dependent factors were applied to correct for the loss of events in which a photon was vetoed by a coincident charged particle. These factors were computed with Monte Carlo simulations based on GEANT [25], using simulated events as input from both the ARC [27] and Lund (Fritiof) [28] event generators. The factors ranged from a maximum of approximately 1.25 at the most forward angles to very close to 1 at the backward angles, and did not depend strongly on which event generator was used. The probability for more than one photon in the same BAF detector was also estimated and determined to be less than 2% at the most forward angles (where it is the largest). Energy resolution, position resolution, and photostatistics were studied and determined to have a negligible effect on the p_T spectra.

IV. INCLUSIVE PHOTON p_T SPECTRA

The inclusive photon $d^2\sigma_\gamma/dydp_T$ cross sections as a function of p_T at the measured y_{NN} rapidities are shown in Fig. 6 for the p -Be data, and Fig. 7 for the p -W data. All corrections described in the previous section have been applied. The spectrum for $p_T < 0.05$ GeV/c is the region of interest for searching for an excess of low p_T photons, and will be discussed in detail in a later section. For $p_T > 0.05$ GeV/c, the spectra are fit well by simple exponentials, although the exponential slope factors vary as a function of rapidity. Table II gives the slope factors in $(\text{GeV}/c)^{-1}$ for the p -Be and p -W data determined from an exponential fit in the range $0.04 \leq p_T \leq 0.6$ GeV/c. The slope factors increase significantly as the rapidity changes from the forward to the backward direction. This is a direct result of the p_T and

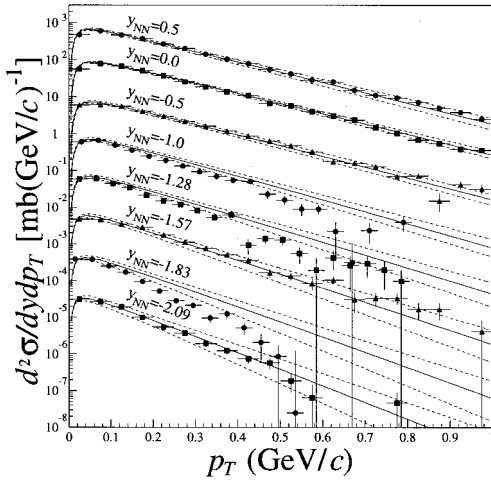


FIG. 6. Inclusive photon cross sections as a function of p_T for different rapidities for p -Be data. The scale on the left gives the appropriate cross section for $y_{NN} = +0.5$. The data for each of the other rapidities have been multiplied incrementally by factors of 0.1 to show the spectra on the same graph. The solid lines give the results of the global π^0 fit described in the text, and the dashed curves indicate the errors on the fit.

rapidity dependence of the π^0 production, which is discussed in the next section.

The inclusive photon $d\sigma_\gamma/dy$ cross sections integrated over p_T are listed for each measured rapidity in Table II and plotted in Fig. 8. The rapidity intervals subtended by the BAF detectors are indicated by the bin widths. Both distributions were fitted by Gaussians, which are shown as smooth curves on the figures. Assuming this Gaussian form for the $d\sigma_\gamma/dy$ distribution, the total inclusive photon cross section σ_γ integrated over rapidity is 350^{+105}_{-35} (sys) mb for p -Be, and 5900^{+900}_{-600} (sys) mb for p -W.

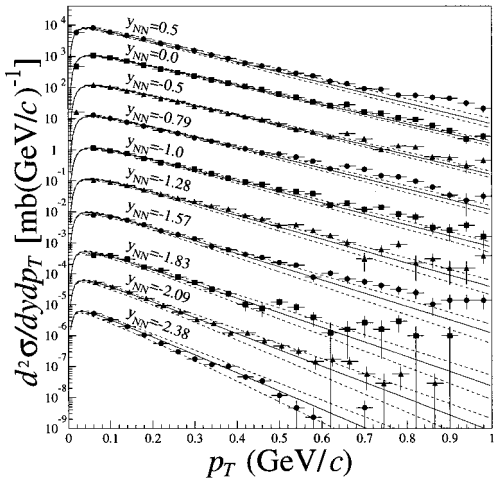


FIG. 7. Inclusive photon cross sections as a function of p_T for different rapidities for p -W data. The scaling of the p_T spectra and the meanings of the lines are the same as in Fig. 6.

V. NEUTRAL PION SPECTRA

A. Reconstructed neutral pions

Although the geometrical acceptance of each BAF detector was very limited, there was a small probability of detecting both photons from a single π^0 decay by measuring one photon in each detector. A small portion of the total data (1896 events) were events with a coincident neutral signal in each of the BAF detectors, which included the events containing a pair of photons from the same π^0 decay. Figure 9 shows the invariant mass distribution for the coincident neutral events, which consists of a slowly varying continuum of random combinations, along with a prominent peak near the π^0 mass. A cut of $p_T > 135$ MeV/c on the photon pair eliminated much of the combinatorial background below the mass peak without significantly affecting the peak itself or the higher mass continuum. After this cut, a polynomial was fitted to the continuum background, and then subtracted from the distribution. A Gaussian function was then fitted to the residual mass spectrum. The peak value gave a mass of 135 MeV/c² (exactly the π^0 mass), and the width was $\sigma_m = 10.5$ MeV/c². This width is consistent with the expected energy and position resolution, and the correct value for the π^0 mass demonstrates the validity of the energy calibration and energy leakage corrections. Unfortunately, the poor statistics do not allow further study of other π^0 properties, such as the rapidity and p_T distributions.

B. Fitted neutral pion spectra

Because of the limited statistics for reconstructed π^0 's, an alternative approach was used to determine the π^0 p_T and rapidity distributions from the inclusive photon data. In principle, given the global photon p_T and rapidity distributions from π^0 decays, one can determine the global π^0 p_T and rapidity spectra using a deconvolution procedure [29]. However, the procedure becomes very complicated with small acceptance slices, and it is subject to numerical difficulties with finite statistics [30].

A preferable procedure, which has been used by other experiments [18], is to assume an analytic function $f_{\pi^0}(y, p_T; a_i)$ for the π^0 distribution $d^2\sigma_{\pi^0}/dydp_T$ which depends on the fit parameters a_i . From the $\pi^0 \rightarrow \gamma\gamma$ decay kinematics, the contribution to the photon $d^2\sigma_\gamma/dydp_T$ can be calculated numerically for any values of y and p_T for the π^0 . The form of the function $f_{\pi^0}(y, p_T)$ can be chosen such that the parameterization for neutral pions is similar to that used to describe charged pions, which has been determined by other experiments at similar energies. Charged pion p_T distributions from p -nucleus collisions at 14.6 GeV/c have been fitted to a function of the form $dN/dp_T \propto p_T \exp[-am_T]$, where $m_T = \sqrt{p_T^2/c^2 + m_{\pi^0}^2}$ is the transverse mass [31]. Charged pion rapidity distributions can generally be fitted with a Gaussian function, $dN/dy \propto \exp[-(y-y_0)^2/(2\sigma^2)]$. The π^0 distribution was therefore parameterized in y and p_T by a Gaussian in rapidity and an exponential in m_T , where the exponential slope parameter depends on rapidity according to the function:

$$f_{\pi^0}(y, p_T) = a_1 p_T \exp[-(a_2 + a_3 y + a_4 y^2) m_T] \times \exp[-(y - a_5)^2 / (2a_6^2)]. \quad (1)$$

TABLE II. Exponential slope factors b in $(\text{GeV}/c)^{-1}$ fitted to the form $d^2\sigma_\gamma/dydp_T = \exp(a-bp_T)$, and $d\sigma_\gamma/dy$ in mb, for p -Be and p -W at various y_{NN} rapidities. The systematic error in the absolute normalization of the $d\sigma_\gamma/dy$ values is estimated to be $(+30\%, -10\%)$ for p -Be, and $(+15\%, -10\%)$ for p -W.

y_{NN}	p -Be		p -W	
	p_T slope $(\text{GeV}/c)^{-1}$	$d\sigma/dy$ (mb)	p_T slope $(\text{GeV}/c)^{-1}$	$d\sigma/dy$ (mb)
+0.50	5.78 ± 0.08	100	6.98 ± 0.06	1440
0.00	5.97 ± 0.07	136	6.50 ± 0.05	2060
-0.50	6.03 ± 0.15	109	6.68 ± 0.08	2270
-0.80			6.84 ± 0.08	2240
-1.00	6.32 ± 0.33	97	7.02 ± 0.10	2020
-1.28	6.95 ± 0.35	86	7.28 ± 0.12	1900
-1.57	7.74 ± 0.33	61	8.18 ± 0.12	1340
-1.83	10.3 ± 0.56	40	10.5 ± 0.81	660
-2.10	10.4 ± 0.58	26	11.1 ± 0.19	650
-2.38			13.7 ± 0.22	530

The function $f_{\pi^0}(y, p_T)$ was used to calculate the photon p_T spectrum at each measured rapidity, and the fit parameters a_i were adjusted to minimize the χ^2 between the calculated spectra and the measured data. The parameters a_i obtained from the fits for the p -Be and p -W data are listed in Table III along with their respective χ^2/DOF (degree of freedom). The fits determine both the π^0 distributions and π^0 decay contributions to the photon spectra at all p_T . The range of photon p_T used in the fits was restricted to $0.05 \leq p_T \leq 0.40$ GeV/ c for p -Be, and $0.05 \leq p_T \leq 0.50$ GeV/ c for p -W. According to simulations with Lund and GEANT, photons in these p_T ranges come almost exclusively from π^0 decays, with little contamination from other sources, as discussed below.

The contribution to the photon p_T spectra below 0.05 GeV/ c due to π^0 decays was *predicted* based on the fits at

higher p_T . The yield of π^0 decay photons falls steeply at low photon p_T because of the nonzero π^0 mass. Low p_T photons from π^0 decays at a given rapidity come primarily (but with relatively low probability) from low $p_T \pi^0$'s approximately 1–2 units away in rapidity. To estimate the π^0 contribution to the low p_T photon spectra accurately, it is necessary to determine the π^0 distribution over a large interval in rapidity. The range of detector angles used for this experiment covered almost 3 rapidity units, which allowed the π^0 distribution function to be fitted over approximately the same range.

Figures 6 and 7 show the high p_T range of the photon $d^2\sigma_\gamma/dydp_T$ spectra. The solid curves superimposed on the data are the photon spectra derived from the π^0 decay fits, and the dashed curves represent the errors on the fit. The curves agree well with the p -Be data at all transverse momenta $p_T < 0.5$ GeV/ c , and all rapidities except $y = -1.83$, and for $p_T < 0.6$ GeV/ c at all rapidities for the p -W data. The p -W data slightly exceed the fits at high p_T for a few rapidities, but this has no effect on the extrapolation of the fits into the low p_T region.

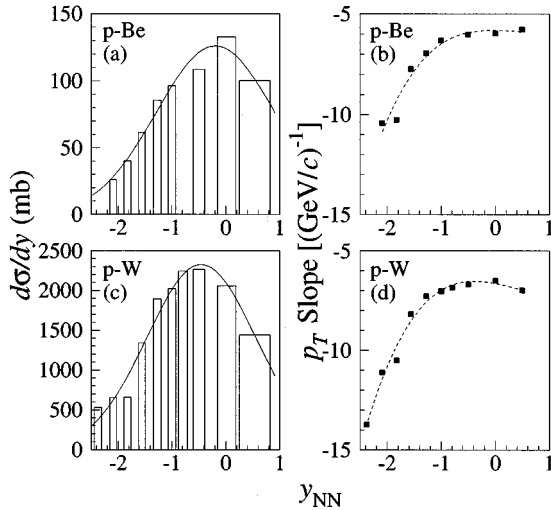


FIG. 8. Inclusive photon cross sections and exponential slopes as a function of y_{NN} for the p -Be and p -W data. In the left panels, the histogram bin heights represent $d\sigma/dy$ in mb, and the bin widths represent the Δy acceptance at each detector position. The points in the right panels represent the fitted exponential slopes in $(\text{GeV}/c)^{-1}$; the dashed lines through the slope points are just to guide the eye. The top two panels are p -Be, and the bottom two are p -W.

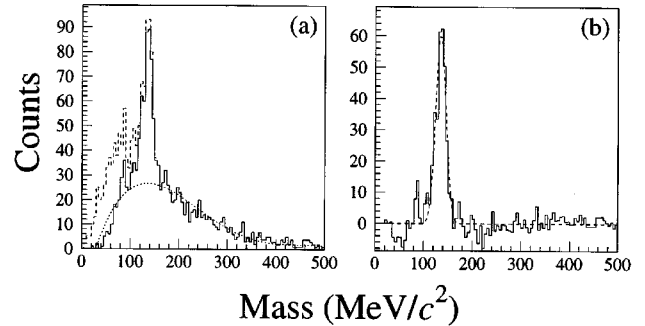


FIG. 9. Invariant mass of coincident photons in BAF1 and BAF2. In panel (a), the dashed curve is the full mass spectrum, the solid curve is the mass spectrum with a cut of $p_T > 135$ MeV/ c , and the dotted curve shows a fit to the background continuum. Panel (b) shows the mass spectrum with the high p_T cut and the background continuum subtracted. The dashed curve is a fit of the peak to a Gaussian function which gives a peak value of 135 MeV/ c^2 and a width of $\sigma_m = 10.5$ MeV/ c^2 .

TABLE III. Values for the a_i parameters of the π^0 distribution functions $d^2\sigma_{\pi^0}/dydp_T = f_{\pi^0}(y,p_T) = a_1 p_T \exp[-(a_2 + a_3 y + a_4 y^2) m_T] \exp[-(y - a_5)^2 / (2a_6^2)]$ (see text).

Parameter	p -Be	p -W
a_1 [mb/(GeV/c)]	4100^{+1300}_{-600}	107000^{+10000}_{-12000}
a_2 (GeV/c ²) ⁻¹	6.53 ± 0.09	7.29 ± 0.07
a_3 (GeV/c ²) ⁻¹	-0.455 ± 0.197	0.246 ± 0.147
a_4 (GeV/c ²) ⁻¹	0.643 ± 0.149	1.24 ± 0.08
a_5	-0.688 ± 0.080	-1.15 ± 0.07
a_6	1.36 ± 0.13	1.49 ± 0.09
χ^2/DOF	1.21	2.02

VI. LOW p_T PHOTON BACKGROUNDS

A. Other hadron decays

The main source of photons in the range $p_T \geq 50$ MeV/c is due to π^0 decays. Other neutral mesons, such as the η , η' , and ω , and certain baryons, such as the Σ^0 , also contribute to the inclusive photon spectrum, but there are virtually no experimental data on the production cross sections for these particles at these energies. Their contribution to the photon spectrum was therefore estimated using the Lund Monte Carlo, which was optimized for use in this energy range [28], in order to determine their photon yields relative to that of π^0 's. Figure 10 shows that the heavier mesons and baryons contribute mainly in the p_T range of a few hundred MeV/c, but are negligible in the region below 50 MeV/c. Therefore, even with a possible large systematic uncertainty on the relative cross sections based on the Lund model, the effect on the low p_T inclusive photon spectrum should be very small.

B. Secondary photons from the target

Another source of background at low p_T is the production of low energy secondary photons in the target. This is not significant in the case of beryllium, but it is a major source of background for tungsten. The main contribution comes from

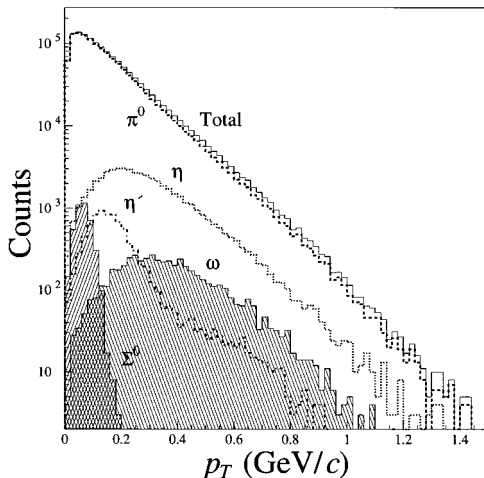


FIG. 10. Hadronic decay contributions from π^0 , η , η' , ω , and Σ^0 to the p -W inclusive photon p_T spectrum at $y_{NN}=0$, as predicted by the Lund Monte Carlo.

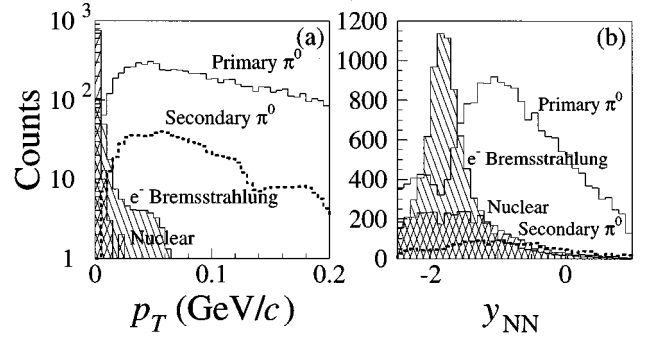


FIG. 11. Left panel: contributions to the p -W inclusive photon spectrum as a function of p_T at $y_{NN}=0$ due to secondary interactions in the target (computed using ARC and GEANT). The curves show the individual contributions due to electron bremsstrahlung, nuclear interactions (primarily n - γ), and secondary π^0 decays, along with the primary π^0 decay contribution. Right panel: secondary photon contributions as a function of rapidity for p -W. The background peak at $y_{NN} = -1.83$ is due to the transverse thickness of the tungsten target ($\sim 2X_0$) near 90° in the laboratory.

π^0 decay photons which convert in the target, producing electron pairs which then radiate low energy photons by bremsstrahlung. This effect is particularly large at rapidities near 90° in the laboratory, where the path length for a photon to escape the target was ~ 7.2 mm ($\sim 2X_0$).

The contribution to the photon spectrum from secondary interactions was estimated using a GEANT simulation (version 3.21), including all relevant physical processes, with particles from the primary interaction simulated using the ARC and Lund event generators. The primary vertices were placed at random positions within the target corresponding to the actual beam spot, and all particles were tracked through the target, where secondary interactions were allowed to occur. Photons from all secondary processes were tracked to the detectors along with any accompanying charged particles. The resulting photon p_T spectra were then computed, taking into account the effect of the charged particle vetos. The simulated p_T spectra of secondary photons were scaled by normalizing the simulated and actual photon spectra in the range $0.05 \leq p_T \leq 0.4$ GeV/c (which are mainly due to π^0 decays), and then subtracted from the real data.

The secondary photon p_T spectrum for the tungsten target at $y_{NN}=0$ is shown in Fig. 11. Bremsstrahlung photons make the major contribution in the p_T region below ~ 50 MeV/c, while other secondary processes such as secondary π^0 's and nuclear interactions contribute much less. Figure 11 also shows how the relative contribution of each secondary process varies with rapidity. The large bremsstrahlung contribution at $y_{NN} = -1.83$ (90° in the laboratory) reflects the high conversion and bremsstrahlung probability for photons passing transversely through the target.

The GEANT 3.21 simulation of the low p_T bremsstrahlung photons exceeded the measured data at laboratory angles near 90° . However, an earlier version of GEANT (3.15) underpredicted the low p_T secondary spectra for the same laboratory angles. The difference was mainly due to the difference in the angular correlation between bremsstrahlung photons and their parent electrons. Version 3.21 gave a weaker correlation, which predicted that fewer bremsstrah-

lung photons would be vetoed by the charged particle veto counters in front of the BaF₂ detectors, while version 3.15 gave a stronger correlation which resulted in a much smaller background subtraction. This resulted in a large systematic uncertainty in the secondary background subtraction for the tungsten data for rapidities less than -1.0 . As a result, these data were not used in the final analysis of the low p_T photon spectra.

C. Hadronic bremsstrahlung

Hadronic bremsstrahlung radiation from charged hadrons produced during the collision is another source of photons at low p_T . It can be calculated classically in the limit of low photon energy using the Low theorem [8]. In this limit, where the photon wavelength exceeds the source size, the hadronic bremsstrahlung depends only on the initial and final charged currents and does not depend on the details of the internal hadronic interaction. This background was estimated using a method similar to that used by others [18]. The number density of photons is given by the formula

$$\frac{d^2N}{d\eta dk_T} = \frac{\alpha k_T}{4\pi^2} \int_0^{2\pi} |J^\mu(\eta, \Phi) J_\mu(\eta, \Phi)| d\Phi, \quad (2)$$

where

$$J^\mu(\eta, \Phi) = \frac{1}{k_T} \left[\sum_f \frac{q_f p_f^\mu}{m_{Tf} \cosh(y_f - \eta) - p_{Tf} \cos(\phi_f - \Phi)} - \sum_i \frac{q_i p_i^\mu}{m_{Ti} \cosh(y_i - \eta) - p_{Ti} \cos(\phi_i - \Phi)} \right]. \quad (3)$$

The quantity $J^\mu(\eta, \Phi)$ is the 4-vector current density expressed in terms of the 4-momenta (p^μ), charge (q), transverse mass (m_T), transverse momentum (p_T), rapidity (y), and azimuthal angle (ϕ) of the initial and final state charged particles, and the pseudorapidity (η) and azimuthal angle (Φ) of the photon. The quantity k_T is the transverse momentum of the photon and α is the fine structure constant. The summations run over all initial and final state particles. However, evaluation of this expression requires the knowledge of the 4-momenta of all incoming and outgoing charged particles in the interaction, but these were not measured in the experiment. Therefore, the 4-vectors of particles in events generated by the Lund and ARC Monte Carlo programs were used to calculate the level of the bremsstrahlung radiation relative to π^0 production. The result was a photon spectrum which varied as $1/k_T$ that could be normalized relative to the spectrum of photons from π^0 decays in the simulated and actual photon spectra in the range $0.05 \leq p_T \leq 0.4$ GeV/c. This spectrum, along with a systematic error estimate based on the difference between the two event generators, will be compared with the measured inclusive photon data in the next section.

D. Neutrons

Neutrons are also a source of background, since a neutron interacting in the BaF₂ crystals can simulate a photon

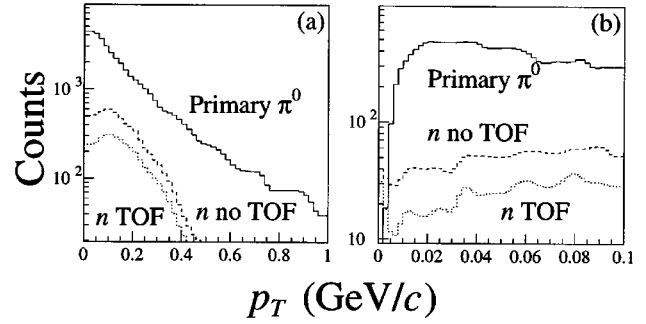


FIG. 12. Contribution to the inclusive photon spectrum for p -W interactions at $y_{NN} = +0.5$ due to neutrons which fail (n no TOF), and survive (n TOF) the time of flight cut ($t < 5.5$ ns), simulated using GEANT and Lund. Photons from primary π^0 's are also shown to indicate the small scale of the neutron contamination. Part (a) gives the p_T spectrum from 0–1 GeV/c and (b) gives the same spectrum from 0–0.1 GeV/c.

shower. However, neutrons with kinetic energies less than ~ 1.3 GeV were removed by the TOF cut. The ratio of the number of neutrons surviving the TOF cut to the total number of photons was estimated using both ARC and Lund and found to be at most 0.28 at $y_{NN} = +0.5$, and negligibly small at backward rapidities. The apparent photon signal produced by neutrons that survived the TOF cut at forward rapidities was estimated using a GEANT simulation of neutrons interacting in the BAF detectors, folded with the spectra of neutrons given by the ARC and Lund event generators. The result, given in Fig. 12 for $y_{NN} = +0.5$, shows that the neutron background makes only a small contribution in the p_T range of a few hundred MeV/c, and is negligible at low p_T .

E. Decay of excited nuclei

Another possible source of low energy photons is ‘‘thermal’’ radiation from the decay of highly excited heavy nuclear fragments produced in the p -W collisions. Two theoretical models [32] were used to estimate the yield of continuum radiation from hot nuclei. The basic photon production mechanism in both these models is internal p - n bremsstrahlung in a thermalized, expanding nucleus. Although the models were developed for intermediate energy nucleus-nucleus collisions, they provide a reasonable estimate of the level of photon production in the target remnant of proton-nucleus collisions. The predicted photon p_T spectrum depends strongly on the assumptions made for the temperature, volume, and lifetime of the nuclear remnant, but for any reasonable temperatures which could be achieved in p -W collisions ($T \leq 15$ MeV), the contribution to the inclusive photon spectrum is negligibly small.

VII. LOW p_T PHOTON SPECTRA

Figures 13, 14, and 15 show the fully corrected photon spectra $d^2\sigma_\gamma/dydp_T$ for p -Be and p -W in the transverse momentum range from $0 \leq p_T \leq 100$ MeV/c. The errors shown on the data points include the statistical errors along with the systematic errors from the various corrections, but do not include the overall systematic error on the normalization of (+30%, -10%) for p -Be, and (+15%, -10%)

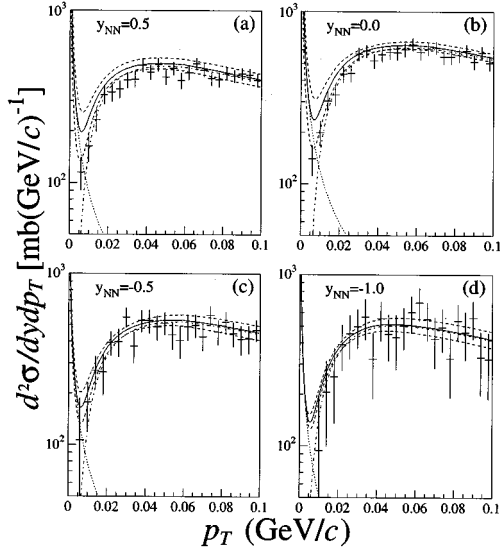


FIG. 13. Inclusive photon cross sections as a function of p_T in the region below 0.1 GeV/c for the p -Be data. The four y_{NN} rapidities +0.5, 0, -0.5, and -1.0 are shown in this figure. The dot-dashed lines give the extrapolation of the π^0 decay contribution from the global π^0 fit described in the text. The dotted lines give the hadronic bremsstrahlung contribution, which rises at low p_T . The solid lines give the sum of π^0 decay plus hadronic bremsstrahlung photons. The dashed lines indicate the errors from the π^0 fit along with the systematic errors from the bremsstrahlung calculation.

for p -W. The curves give the contributions to the photon spectra from π^0 decays extrapolated to low p_T from the global fit to the π^0 rapidity and p_T distribution, along with the calculated hadronic bremsstrahlung. The error band around the curve represents the uncertainty in the π^0 and bremsstrahlung contributions due to the π^0 fit and the model de-

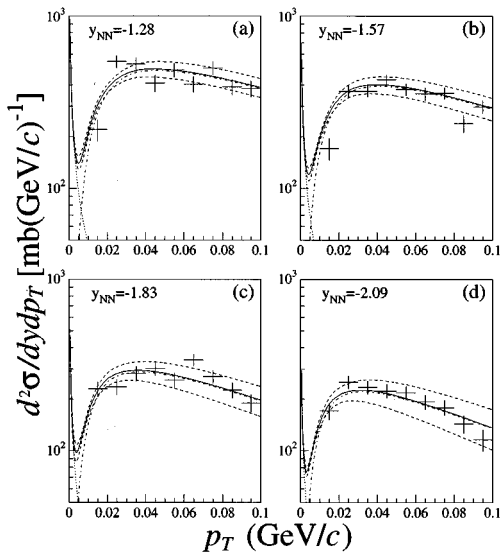


FIG. 14. Inclusive photon cross sections as a function of p_T in the region below 0.1 GeV/c for the p -Be data. The four y_{NN} rapidities -1.28, -1.57, -1.83, and -2.09 are shown in this figure. The lines are the same as in Fig. 13.

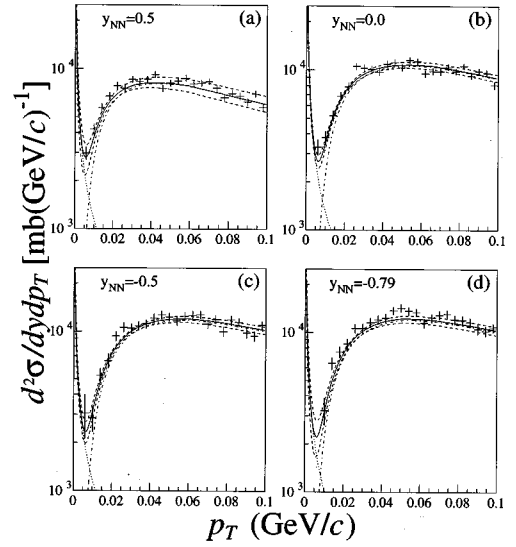


FIG. 15. Inclusive photon cross sections as a function of p_T in the region below 0.1 GeV/c for the four forward y_{NN} rapidities +0.5, 0, -0.5, and -0.8 for the p -W data. The lines are the same as in Fig. 13.

pendence of the bremsstrahlung calculation. The π^0 upper and lower error curves were generated by sampling the $f_{\pi^0}(y, p_T; a_i)$ function fit parameters a_i over Gaussian distributions around their best-fit values, using the errors on the fit parameters for the widths of the Gaussians. The upper and lower bremsstrahlung curves are those predicted using the charged particle distributions from the Lund and ARC event generators, respectively, and the middle curve is the average of the two. All eight rapidities are shown for p -Be, but only the four most forward rapidities ($y_{NN} = +0.5, 0, -0.5,$ and -0.8) are shown for p -W, because of the large systematic uncertainty in the secondary background subtraction for the p -W data at laboratory angles near 90° .

No significant excess is seen in either the p -Be or p -W data above the estimated π^0 and hadronic bremsstrahlung contributions in the p_T range from $12 \leq p_T \leq 52$ MeV/c, where other experiments have reported such a signal, at any of the measured rapidities. This is shown quantitatively in Table IV, which gives the photon cross sections $d\sigma_\gamma/dy$ summed over p_T in the range $12 \leq p_T \leq 52$ MeV/c at each rapidity for the data and the calculated background, along with the difference in mb. In all cases, the residual signal is consistent with zero within the estimated error.

For the p -W data from $-0.9 \leq y_{NN} \leq 0.8$, the limit on excess low p_T photons can be quantified in terms of a factor F times the calculated hadronic bremsstrahlung. The fitted π^0 contributions to the photon spectra were subtracted from the photon $d^2\sigma/dy dp_T$ cross sections for the four forward-most p -W rapidities. The residual photon data were summed (weighted by the Δy at each detector position) to obtain $d\sigma/dp_T$. The χ^2 between the residual data and the bremsstrahlung was calculated, propagating the respective errors from the data, the π^0 fit, and the bremsstrahlung. This gave $\chi^2 = 23.0$ with 12 degrees of freedom, for 12 data points from $4 \leq p_T \leq 52$ MeV/c (with no free parameters). The con-

TABLE IV. Low p_T photon cross sections $d\sigma_\gamma/dy$, summed over the p_T interval $12 \leq p_T \leq 52$ MeV/c, the calculated hadron decay plus hadron bremsstrahlung background cross sections, summed over the same p_T interval, and the residual cross section, for p -Be and p -W.

y_{NN}	p -Be low $p_T d\sigma_\gamma/dy$ (mb)			p -W low $p_T d\sigma_\gamma/dy$ (mb)		
	Data	Background	Difference	Data	Background	Difference
+0.50	15.5 ± 1.6	17.7 ± 1.4	-2.2 ± 2.2	315 ± 18	298 ± 20	18 ± 28
0.00	19.7 ± 2.0	22.0 ± 1.4	-2.2 ± 2.4	373 ± 20	361 ± 13	13 ± 23
-0.50	17.3 ± 3.0	17.9 ± 1.2	-0.6 ± 3.2	406 ± 28	381 ± 13	25 ± 30
-0.80				431 ± 30	391 ± 18	40 ± 35
-1.00	16.5 ± 5.3	17.7 ± 1.2	-1.2 ± 5.5			
-1.28	17.1 ± 3.5	17.1 ± 1.4	0.0 ± 3.7			
-1.57	13.4 ± 2.2	14.4 ± 1.4	-1.0 ± 2.6			
-1.83	10.6 ± 2.0	10.8 ± 1.2	-0.2 ± 2.4			
-2.10	8.7 ± 1.6	8.5 ± 1.2	0.2 ± 2.0			

fidence level for this χ^2 is $C.L.(\chi^2) = 0.028$.¹ Introducing F as the factor multiplying the bremsstrahlung, the best $\chi^2 = 8.95$ (with 11 degrees of freedom) was obtained with $F = 1.62$, giving a $C.L.(\chi^2) = 0.63$. (One degree of freedom is lost by introducing the factor F .) All $F \geq 2.65$ give a $C.L.(\chi^2) < 10^{-2}$; thus the data set a limit of < 2.65 times bremsstrahlung at the 99% confidence level. These results are plotted in Fig. 16, which shows the residual p -W photon data and the bremsstrahlung curves with $F = 1$, 1.62, and 2.65. The limit for p -Be is even more stringent, since most of the lowest p_T data points in Figs. 13 and 14 lie below the sum of the π^0 and bremsstrahlung curves.

These results indicate no significant excess of low p_T photon production above the level of hadronic bremsstrahlung in either the p -Be or p -W data in the p_T range $4 \leq p_T \leq 52$ MeV/c. This agrees with the results of Ref. [15], which claimed no photon excess for $p_T \leq 20$ MeV/c, and Ref. [18], which claimed less than a factor of 2 times bremsstrahlung for $p_T \approx 10$ MeV/c, but does not agree with Refs. [5] and [6], which saw an excess five times greater than hadronic bremsstrahlung for $p_T \leq 40$ –60 MeV/c. The fact that no excess was seen in p -Be at either 18 GeV or 450 GeV (measured in Ref. [18]), implies that any explanation of this discrepancy based on energy dependence is unlikely. Since p -Be collisions are very similar to p - p , K - p , and π - p interactions, it further seems unlikely that the discrepancy between the null observations and those in Refs. [5] (K^+ - p) and [6] (π^+ - p) could be due to the differences in the projectile. In addition, the p -W data show that there is no significant A dependence for this effect. Finally, it should be noted that the purported excess of low mass lepton pairs resulting from soft virtual photon decays can now probably be explained by conventional means [21]. It is therefore difficult to substantiate any reported excess in the yield of soft real photons based on an analogous phenomenon in low mass lepton pairs.

VIII. CONCLUSIONS

Inclusive photon spectra $d^2\sigma/dydp_T$ have been measured in p -Be and p -W interactions at 18 GeV/c in the p_T range

¹ $C.L.(\chi^2) = \int_{\chi^2}^{\infty} f(z;n) dz$, where $f(z;n)$ is the probability density function for χ^2 with n degrees of freedom.

from a few MeV/c up to ~ 1 GeV/c at various rapidities in the interval $-2.4 \leq y_{NN} \leq +0.5$. Photon production for $p_T \geq 50$ MeV/c is dominated by π^0 decay, and the shape of the spectra agrees well with that expected from π^0 production. Photon production at very low p_T (≤ 20 MeV/c) has a significant contribution from hadronic bremsstrahlung from the charged particles produced in the collision, which can be calculated in the soft photon limit. The photon spectrum in the range $12 \leq p_T \leq 52$ MeV/c agrees well with that expected from the sum of π^0 decays and hadronic bremsstrahlung. Within errors, there is no evidence for any anomalous excess of soft photons in this p_T region in p -Be interactions at any rapidity, or in p -W interactions at rapidities $y_{NN} \geq -1$. The p -W data set a limit < 2.65 times bremsstrahlung for any excess, at the 99% confidence level. These results are consistent with those obtained at higher energies in p -Be interactions [18], and at lower energies in p - p interactions [15], but do not agree with the large excess of soft photon production above the level of hadronic bremsstrahlung seen in K^+ - p and π^+ - p interactions at higher energies [5,6].

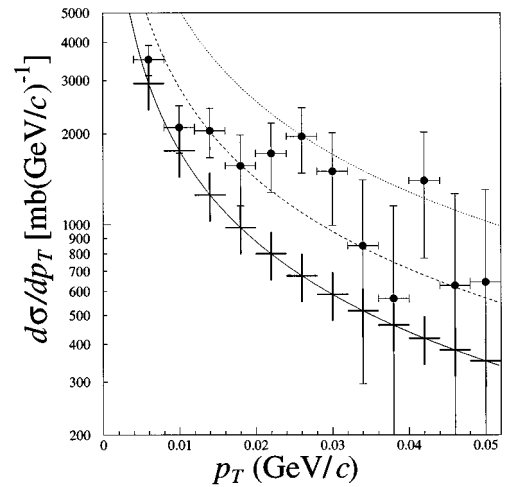


FIG. 16. Data (filled circles) are the p -W photon $d^2\sigma/dydp_T$ cross section from $0.004 \leq p_T \leq 0.052$ GeV/c, summed over $-0.9 \leq y_{NN} \leq +0.8$, with the fitted π^0 contribution subtracted. The lower (solid) curve and crosses is the calculated bremsstrahlung cross section with errors ($F = 1$). The middle (dashed) curve is $F = 1.62$ times the calculated bremsstrahlung (the best χ^2), and the upper (dotted) curve is $F = 2.65$ times bremsstrahlung, the 99% confidence level limit.

ACKNOWLEDGMENTS

We gratefully thank the members of the E814 Collaboration for their cooperation and help in carrying out this experiment, and for the use of their beamline and data acquisition system. We thank Felix Obenshain and Glenn Young of

ORNL for providing the hadron calorimeter. We also thank the AGS staff for providing the beam and other essential facilities. This work was supported in part under Department of Energy Contracts No. DE-AC02-CH7600016 and No. DE-FG02-88ER40412.

-
- [1] M. Diakonou *et al.*, Phys. Lett. **87B**, 292 (1979); A.L. Angelis *et al.*, *ibid.* **94B**, 106 (1980); T. Akesson *et al.*, *ibid.* **123B**, 367 (1983); T. Akesson *et al.*, *ibid.* **158B**, 282 (1985).
- [2] WA80 Collaboration, T. Awes *et al.*, Nucl. Phys. **A590**, 81c (1995).
- [3] J.D. Bjorken and H. Weisberg, Phys. Rev. D **24**, 24 (1981).
- [4] R.C. Hwa and K. Kajantie, Phys. Rev. D **32**, 1109 (1985).
- [5] P.V. Chliapnikov *et al.*, Phys. Lett. **141B**, 276 (1984).
- [6] F. Botterick *et al.*, Z. Phys. C **51**, 541 (1991).
- [7] J.D. Jackson, *Classical Electrodynamics*, 2nd ed. (Wiley, New York, 1975).
- [8] F.E. Low, Phys. Rev. **110**, 974 (1958).
- [9] E.V. Shuryak, Phys. Lett. B **231**, 175 (1989); Phys. Rev. D **42**, 1764 (1990).
- [10] V. Cerny, P. Lichard, and J. Pisut, Z. Phys. C **31**, 163 (1986); V. Cerny *et al.*, *ibid.* **31**, 163 (1989).
- [11] P. Lichard, Report No. SUNY-NTG-94-41, 1994.
- [12] I.V. Ajienco *et al.*, Nucl. Phys. **B162**, 61 (1980).
- [13] J.J. Aubert *et al.*, Report No. CERN-EP/88-33.
- [14] S. Abatzis *et al.*, Nucl. Phys. **A525**, 487 (1991); S. Banerjee *et al.*, Report No. CERN-PPE/92-218 (1992).
- [15] A.T. Goshaw *et al.*, Phys. Rev. Lett. **43**, 1065 (1979).
- [16] T. Akesson *et al.*, Phys. Rev. D **36**, 2615 (1987).
- [17] T. Akesson *et al.*, Phys. Rev. D **38**, 2687 (1988).
- [18] J. Antos *et al.*, Z. Phys. C **59**, 547 (1993).
- [19] K.J. Anderson *et al.*, Phys. Rev. Lett. **37**, 799 (1976); J. Ballam *et al.*, *ibid.* **37**, 1207 (1978); K. Bunnell *et al.*, *ibid.* **40**, 136 (1978); B. Haber *et al.*, Phys. Rev. D **22**, 2107 (1980); A.T. Goshaw *et al.*, *ibid.* **24**, 2829 (1981); S. Mikamo *et al.*, Phys. Lett. **106B**, 428 (1981); D. Blockus *et al.*, Nucl. Phys. **B201**, 205 (1982); M.R. Adams *et al.*, Phys. Rev. D **27**, 1977 (1983).
- [20] HELIOS Collaboration, J. Schukraft *et al.*, Nucl. Phys. **A498**, 79c (1989).
- [21] HELIOS Collaboration, U. Goerlach *et al.*, Nucl. Phys. **A544**, 109c (1992).
- [22] I. Tserruya, Nucl. Phys. **A590**, 127c (1995).
- [23] D. Lissauer *et al.*, Nucl. Phys. **A566**, 451c (1994).
- [24] T. Awes *et al.*, Nucl. Instrum. Methods A **311**, 241 (1992).
- [25] R. Brun *et al.*, GEANT 3.15 Users Guide, Report No. CERN DD/EE/84-1, revised 92-1 (1992).
- [26] Robert Clark, Ph.D. thesis, Vanderbilt University, Nashville, TN, 1996.
- [27] Y. Pang *et al.*, Phys. Rev. Lett. **68**, 2743 (1992); Y. Pang *et al.*, Nucl. Phys. **A544**, 435c (1992).
- [28] Lund Fritiof Monte Carlo, version 1.7, modified for AGS energies by the E802 Collaboration (J. Costales, E802 Internal Report No. E-802-MEM-8, 1988).
- [29] R.M. Sternheimer, Phys. Rev. **99**, 277 (1955); R.G. Glasser, Phys. Rev. D **6**, 1993 (1972); G.I. Kopylov, Nucl. Phys. **B52**, 126 (1973).
- [30] J. Antos, Nucl. Instrum. Methods A **249**, 241 (1986).
- [31] T. Abbott *et al.*, Phys. Rev. Lett. **66**, 1567 (1991); T. Abbott *et al.*, *ibid.* **45**, 3906 (1992).
- [32] H. Nifenecker and J.P. Bondorf, Nucl. Phys. **A442**, 478 (1985); D. Neuhauser and S.E. Koonin, *ibid.* **A462**, 163 (1987).